

# Apertureless scanning near-field optical microscopy: a comparison between homodyne and heterodyne approaches

Lewis Gomez

Chemistry Division and Center for Nanoscale Materials, Argonne National Laboratory, 9700 South Cass Avenue, Argonne, Illinois 60439

Renaud Bachelot

Chemistry Division and Center for Nanoscale Materials, Argonne National Laboratory, 9700 South Cass Avenue, Argonne, Illinois 60439, and Laboratoire de Nanotechnologie et d'Instrumentation Optique, Institut Delaunay CNRS FRE 2848, Université de Technologie de Troyes, 12, rue Marie Curie, BP 2060, 10010 Troyes Cedex, France

Alexandre Bouhelier,\* Gary P. Wiederrecht, Shih-hui Chang, and Stephen K. Gray

Chemistry Division and Center for Nanoscale Materials, Argonne National Laboratory, 9700 South Cass Avenue, Argonne, Illinois 60439

Feng Hua, Seokwoo Jeon, and John A. Rogers

Department of Materials Science and Engineering, Department of Chemistry, University of Illinois at Urbana-Champaign, Urbana, Illinois 61801

Miguel E. Castro

Department of Chemistry, University of Puerto Rico at Mayaguez, Mayaguez, Puerto Rico

Sylvain Blaize, Ilan Stefanon, Gilles Lerondel, and Pascal Royer

Laboratoire de Nanotechnologie et d'Instrumentation Optique, CNRS FRE 2671, Université de Technologie de Troyes, 12, rue Marie Curie, BP 2060, 10010 Troyes Cedex, France

Received July 15, 2005; revised September 26, 2005; accepted October 17, 2005; posted November 17, 2005 (Doc. ID 63448)

In coherent homodyne apertureless scanning near-field optical microscopy (ASNOM) the background field cannot be fully suppressed because of the interference between the different collected fields, making the images difficult to interpret. We show that implementing the heterodyne version of ASNOM allows one to overcome this issue. We present a comparison between homodyne and heterodyne ASNOM through near-field analysis of gold nanowells, integrated waveguides, and a single evanescent wave generated by total internal reflection. The heterodyne approach allows for the control of the interferometric effect with the background light. In particular, the undesirable background is shown to be replaced by a controlled reference field. As a result, near-field information undetectable by a homodyne ASNOM is extracted by use of the heterodyne approach. Additionally, it is shown that field amplitude and field phase can be detected separately. © 2006 Optical Society of America

OCIS codes: 180.5810, 110.2990.

## 1. INTRODUCTION

Since the first results of Pohl *et al.*,<sup>1</sup> scanning near-field optical microscopy (SNOM) has provided optical resolution below the diffraction limit using primarily aperture probes produced from tapered optical fibers.<sup>2–4</sup> Wavelength cutoff effects and difficulties with the fabrication of probes are the primary limits of the use of such probes. An alternative technique uses a homogenous probe that is generally made of a metal or semiconductor.<sup>5–13</sup> This SNOM approach is called apertureless SNOM or ASNOM. It can also be called scattering-type SNOM as a reminder

that the tip extremity acts like a Mie–Rayleigh scattering particle. The reader is referred to a recent review on ASNOM by Patané *et al.*<sup>12</sup>

Generally developed from atomic force microscopy (AFM), ASNOM uses an AFM tip as a SNOM probe that acts as a nanoantenna to scatter the optical near field of the sample. This SNOM approach presents several advantages discussed in Ref. 12, and its impact as a powerful tool for nano-optical characterization continues to increase. For example, it enables nano-optics to be performed over a wider range of wavelengths including

infrared thermal radiation.<sup>14,15</sup> However, even though ASNOM already allows for nanometer-scale physical studies, some efforts are still needed to understand and experimentally control the process of image formation. The present paper addresses these issues.

In ASNOM, external conventional optics (fibers or objectives) allow for far-field illumination and detection. Consequently, background optical fields that are not related to the field scattered by the tip end can be collected. For instance, scattering from defects located within the overall detection area can give rise to large signals responsible for an undesired background. Several methods have been proposed to extract the signal issued from the local interaction between the tip end and the sample surface. These include tip-to-sample distance modulation with lock-in detection,<sup>9–15</sup> demodulation at the high harmonics of the modulation frequency,<sup>16,17</sup> the use of fluorescent active centers integrated at the tip extremity,<sup>18,19</sup> and the excitation of local tip field enhancement at the tip apex.<sup>20</sup> In many experiments, these methods have permitted the extraction of near-field components in the presence of a high level of background field. On the other hand, numerous authors have mentioned that, in the case of light–matter elastic interaction, the background field cannot be fully suppressed because of the coherent superposition of the different collected fields. Consequently, the near-field contrast becomes complicated by interference effects appearing in the images.

Recently, a detailed study of this interferometric effect was proposed by Aubert *et al.*<sup>21</sup> The conclusion of this study is of importance: in coherent ASNOM, both the nature and the behavior of the signal are dramatically dependent on tip environment as well as tip position on the sample surface. This sensitivity originates from the interference between the field scattered by the tip and the background scattered field. Generally speaking, the SNOM signal can describe either the near-field intensity or the complex field amplitude derived from the interferometric effects, but usually there is a subtle mixing of both terms. The effective weight of the interferometric term in the signal depends on the experimental conditions including tip position with regard to the detector and the surrounding scattering structures. This homodyne ASNOM, whereby the scattering from the sample is collected along with the scattering from the tip–sample interaction without additional manipulation, can make ASNOM imaging difficult to interpret. Aubert *et al.* concluded that, despite the richness of the signal, the effect of the interferometric term cannot be fully controlled or eliminated with this type of ASNOM configuration. The authors recommended that the heterodyne version of the ASNOM should be preferentially used. Keilmann and coworkers were the first to use heterodyne ASNOM.<sup>11,22,23</sup> They demonstrated separate detection of amplitude and phase with a resolution of 20 nm in both the visible and the infrared. References 11, 22, and 23 present brief but clear demonstrations of the capability of the heterodyne ASNOM. However, the intrinsic interferometric effect in homodyne ASNOM was not studied, and no comparison between the homodyne and the heterodyne approaches was proposed.

In Ref. 21, homodyne ASNOM was analyzed through evidence of uncontrollable interferometric effects. In this

paper, we present an extensive comparison between the two versions of ASNOM, i.e., the traditional homodyne configuration and the heterodyne approach. We show that the heterodyne approach clearly allows for the control of the interferometric effect between scattering from the tip and a background field. In particular, the undesirable background is shown to be replaced by a controlled reference field. As a result, near-field information undetectable by homodyne ASNOM is extracted by use of the heterodyne approach.

The article is divided into the three following sections. In Section 2, we theoretically describe both homodyne and heterodyne ASNOM. This description is detailed and will allow us to comment on the experimental data. In particular, most of the calculated terms will be experimentally illustrated. In Section 3, we present the experimental apparatus. Next, in Section 4, near-field images obtained with the two ASNOM configurations are presented, analyzed, and compared with each other. These images allow us to observe the intrinsic interferometric effect of the homodyne configuration and to show how the heterodyning controls this effect. In particular, we show that, although the homodyne ASNOM signal can describe nearly randomly either the field intensity or the complex field amplitude, the heterodyne mode provides independently the amplitude and the phase information. The studies were performed on metal nanowells, integrated waveguides, and a single evanescent wave generated by total internal reflection.

## 2. HOMODYNE AND HETERODYNE ASNOM

### A. Homodyne ASNOM

Figure 1(a) represents schematically a typical homodyne ASNOM where both illumination and detection occur through far-field geometries. The tip used is a tapping-mode atomic force microscope probe vibrating vertically above the sample at a frequency  $f$  with an amplitude of a few tens of nanometers. The probe is placed a few nanometers from the sample surface. The sample–tip junction is illuminated with a monochromatic field at frequency  $\omega$ . The light elastically scattered by the tip extremity in near-field interaction with the sample’s evanescent field is far-field detected with a microscope objective and is referred to as  $E_t$ . Owing to the far-field detection, fields other than the field scattered by the tip end have to be taken into account. For this discussion we refer to this general background field as  $E_b$ , which originates from scattering occurring at the sample surface.  $E_b$  would be detected even without the presence of the tip. Let us consider only elastic optical light–matter interactions. In other words, let us suppose that the electromagnetic frequency  $\omega$  is the same for all the involved fields.  $E_b$  and  $E_t$  are characterized by their respective amplitude and phase:  $(|E_b|, \phi_b)$  and  $(|E_t|, \phi_t)$ . The far-field-detected intensity  $I$  is a result of the coherent interference between  $E_b$  and  $E_t$ :

$$I = (E_b + E_t)(E_b^* + E_t^*), \quad (1)$$

where  $E^*$  is the complex field conjugated to  $E$ . Hence,

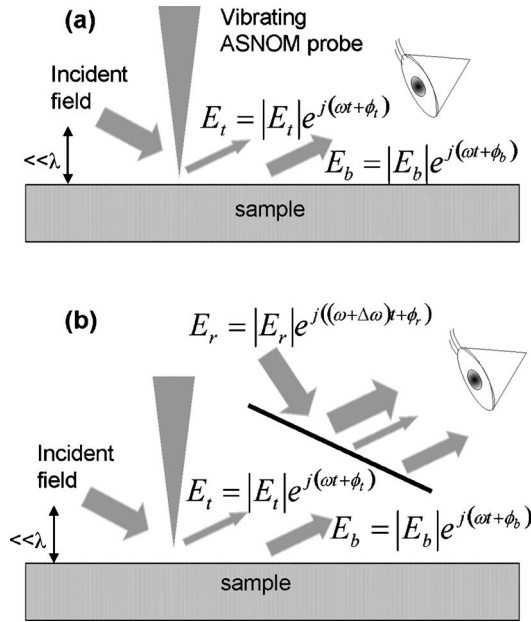


Fig. 1. (a) Schematic configuration of a homodyned ASNOm. The detected light is the coherent superposition of the field scattered by the tip  $E_t$  and a background field  $E_b$  originating from the sample. (b) Schematic configuration of heterodyned ASNOm where a frequency-shifted reference field  $E_r$  is added to control the background signal.

$$\begin{aligned}
 I &= \{|E_b| \exp[j(\omega t + \phi_b)] + |E_t| \exp[j(\omega t + \phi_t)]\} \\
 &\quad \times \{|E_b| \exp[-j(\omega t + \phi_b)] + |E_t| \exp[-j(\omega t + \phi_t)]\} \\
 &= |E_b|^2 + |E_t|^2 + 2|E_b||E_t| \cos(\phi_t - \phi_b). \quad (2)
 \end{aligned}$$

Let us consider that  $I$  is lock-in detected at the tip vibration frequency  $f$  or at its harmonics  $nf$ , where  $n$  is an integer.<sup>16,17</sup> Since the first term of Eq. (2) corresponds to the intensity of the background field that is not modulated by the tip, it is, to a first approximation, filtered out by lock-in detection. The second term of Eq. (2) is the intensity of  $E_t$ , which is the field of interest. It is expected to be modulated at  $nf$ . The third term is the interference term. It is also time varying and can be detected by lock-in detection at  $nf$ . The intensity after the lock-in detection is thus

$$I = |E_t|^2 + 2|E_b||E_t| \cos(\phi_t - \phi_b). \quad (3)$$

Equation (3) highlights the double nature of the ASNOm signal, which can describe the field intensity or the complex field amplitude or, more generally, a subtle combination. In the case of a rough, highly scattering sample,  $|E_b| \gg |E_t|$ , and the second term of Eq. (3) dominates. The detected intensity then consists primarily of the complex near field, and the ASNOm signal contains both phase and amplitude information. In other, less common cases,  $|E_t|^2$  can become significant with regard to the background field. This scenario is conceivable, for example, if the probe detects a single resonant metal nanoparticle deposited on a clean and smooth surface.<sup>13</sup> In this case, the ASNOm is expected to be mainly sensitive to the near-field intensity. The main issue that is highlighted by Eq. (3) is the dependence of the signal on  $E_b$  and  $\phi_b$ , which are not controllable and can even vary during scanning. This

issue has been discussed and illustrated experimentally in Ref. 21. As a result, the nature of the SNOM signal is random and variable during scanning, making the image difficult to interpret.

It should be noted that a high degree of coherence is not a prerequisite to ensure the above interference. The intrinsic interferometer shown in Fig. 1(a) actually involves a small difference of optical paths between  $E_t$  and  $E_b$ . As a result, even light sources with a small coherence length can produce this interference effect. Most of the ASNOm results published so far in the literature are likely to be highly interferometric.<sup>21,24</sup> It is also likely that most of the ASNOm results published so far have, perhaps unwittingly, taken advantage of the interferometric effect because  $|E_b|$  acts as an enhancement factor with regard to  $|E_t|$ , as shown in Eq. (3).

## B. Heterodyne ASNOm

The heterodyne version of the ASNOm appears to be necessary to control the above-described effect. The main idea is illustrated in Fig. 1(b). It essentially replaces the uncontrolled background field with a controllable reference field ( $E_r, \phi_r$ ) that is frequency shifted by  $\Delta\omega$  relative to  $E_t$ . A new lock-in frequency is then used to eliminate the variable background field.

This method can be understood by considering the interference among three fields instead of two: the field of the tip (the field of interest), the background field, and the reference field. As a result, the far-field-detected intensity becomes

$$I = (E_b + E_t + E_r)(E_b^* + E_t^* + E_r^*), \quad (4)$$

which leads to six intensity terms:

$$\begin{aligned}
 I &= I_1 + I_2 + I_3 + I_4 + I_5 + I_6 \\
 &= |E_b|^2 \\
 &\quad + |E_r|^2 \\
 &\quad + |E_t|^2 \\
 &\quad + 2|E_b||E_t| \cos(\phi_b - \phi_t) \\
 &\quad + 2|E_b||E_r| \cos(\Delta\omega t + \phi_r - \phi_b) \\
 &\quad + 2|E_t||E_r| \cos(\Delta\omega t + \phi_r - \phi_t). \quad (5)
 \end{aligned}$$

In Eq. (5), the first three terms ( $I_1, I_2, I_3$ ) correspond to the respective intensities of the different fields. Among them, only  $I_3 = |E_t|^2$  is time varying and can be extracted by lock-in detection at frequencies  $nf$ ,<sup>16,17</sup> thereby filtering out  $|E_b|^2$  and  $|E_r|^2$ . The fourth term ( $I_4$ ) corresponds to the interference between the background field and the field scattered by the tip. This term has been discussed in Subsection 2.A and is modulated by the tip at  $nf$  frequencies.  $I_5$ , the fifth term, results from the interference between the background field and the reference field. This term beats at a  $\Delta\omega$  frequency. Experimentally,  $I_5$  is used to adjust the interferometer alignment by observation of the  $\Delta\omega$  beating with an oscilloscope. The sixth term,  $I_6$ , is the term of interest. It corresponds to the interference between  $E_t$  and the reference field, regardless of the background field. It can be extracted by a different lock-in de-

tection frequency of  $nf - \Delta\omega/2\pi$ . Keeping in mind that  $|E_t|$  is modulated by the tip oscillation, we can actually express  $I_6$  as a Fourier series:

$$I_6 = A_1|E_t|\cos(\Omega t)|E_r|\cos(\Delta\omega t + \phi_r - \phi_t) \\ + A_2|E_t|\cos(2\Omega t)|E_r|\cos(\Delta\omega t + \phi_r - \phi_t) \\ + A_3|E_t|\cos(3\Omega t)|E_r|\cos(\Delta\omega t + \phi_r - \phi_t) + \dots, \quad (6)$$

where  $\Omega = 2\pi f$ .

In Eq. (6) the weights  $A_i$  of the Fourier terms are easily calculable if the detection of a single evanescent wave (generated by total internal reflection) is performed.<sup>21,25,26</sup> In the case of evanescent fields generated by diffraction by small objects, the problem is more complex because the near field detected by the tip can be viewed as a continuous spectrum of plane waves.<sup>27</sup> If we focus our attention, for example, on the second term of Eq. (6), we have

$$I_6\alpha|E_t||E_r|\cos[(2\Omega \pm \Delta\omega)t + \phi_r - \phi_t]. \quad (7)$$

Expression (7) shows that it is possible to obtain valuable data by performing lock-in detection at a frequency  $(2\Omega - \Delta\omega)/2\pi$ . The amplitude channel of the lock-in amplifier now provides the amplitude of the tip field, without any phase information, independently of the background field. In addition, this amplitude is enhanced by an adjustable factor  $|E_r|$ . On the other hand, the phase channel provides pure phase information on the tip field whose origin is the phase of the reference field, thus yielding valuable information on the phase delay of the optical near field relative to the reference field. Such information can be valuable for determining the physical origin of the optical near field. For example, in the case of metal nanostructures, phase information can reveal if the evanescent field is due to a plasmon resonance or if interparticle electronic coupling is occurring.

### 3. EXPERIMENTAL SETUP

Figure 2 shows schematically the two experimental configurations that were used to address the above issues. Figure 2(a) represents a backscattering reflection-mode configuration similar to that developed by Keilmann and co-workers.<sup>11,22,23</sup> The general setup has been developed from a commercial atomic force microscope (Multimode from Digital Instruments with a Nanoscope IIIA controller) to which a Michelson interferometer has been integrated. A laser beam delivered by a single-mode krypton laser ( $\lambda = 647.4$  nm) is split by the beam splitter BS1 into two beams. The first beam is frequency shifted by  $\Delta\omega$  with two crossed acousto-optical modulators (AOM1 and AOM2).  $\Delta\omega$  is set in the few hundreds of kHz range with a precision of 10 kHz. This first beam is launched into a single-mode optical fiber by the objective lens L1 and is defined as the reference field  $E_r$ . The second beam emerging from BS1 is directed to the objective lens O [numerical aperture (N.A.) = 0.28, focal length 10 mm], which focuses the light onto the extremity of a silicon AFM tip (Mikromasch, NSC15) in interaction with the sample. The axis of the objective has an angle of  $15^\circ$  with the sample surface. The tip operates in tapping-mode AFM, vibrating

perpendicular to the sample with a  $f$  frequency of  $\sim 300$  kHz and an amplitude of  $\sim 40$  nm. As discussed in Section 2, the local tip-sample-light interaction leads to scattered light ( $E_t + E_b$ ) that is collected by the same objective lens (reflection-mode backscattering configuration) and coupled into the optical fiber by the objective L1. The single-mode optical fiber (core diameter  $\sim 4$   $\mu\text{m}$ ) acts as an efficient means to force the interference among the three involved fields. Since the fiber operates in single mode, only one wave vector is guided, making the different field wave vectors automatically collinear to each other. The performance of the interferometer has been demonstrated by observation of the  $\Delta\omega$  beating [corresponding to the fifth term of Eq. (5)], with an oscilloscope. This beating is easily observable if a highly scattering sample is used.

The focal length of L1 has been chosen with regard to the objective O so that the image of the  $4$   $\mu\text{m}$  fiber core by the two lenses (L1,O) has a size comparable with the diffraction spot of the objective O (diameter =  $1.22\lambda/\text{N.A.} = 2.8$   $\mu\text{m}$ ). We choose a 20 mm focal-length lens L1, allowing for a confocal detection of the light scattered only within a few micrometers of the tip end. The CCD camera shown in Fig. 2(a) allows for easy observation of the tip, sample, and incident laser spot. The confocal zone of detection can be visualized by one's coupling an additional laser beam from the other extremity of the fiber (not shown in the figure). With translation stages and kinematic mirrors mounts, it is possible to adjust the position of zones of illumination and detection at the apex of the tip. The polarization state of the incident field is linear and can be controlled by a rotating half-wave plate (not shown in Fig. 2). The polarization state of  $E_r$  is also adjusted to maximize the visibility of the interference signal at  $\Delta\omega$ . After detection of the light by a photomultiplier (PM), the SNOM signal is obtained by lock-in detection at various frequencies ( $f, 2f, 2f - \Delta\omega/2\pi, \dots$ ). The tapping-mode AFM signal is simultaneously recorded.

Figure 2(b) shows an alternative heterodyned configuration where the illumination of the sample occurs through total internal reflection. The detection path is essentially identical to that of Fig. 2(a).

### 4. NEAR-FIELD IMAGING: HOMODYNE VERSUS HETERODYNE

#### A. Amplitude Imaging

Figure 3 illustrates the interferometric nature of the signal that is typically collected with the homodyne ASNM configuration where fringes dominate the contrast. The sample consists of a 50 nm high, 300 nm wide gold wire produced by electron-beam lithography. The sample was illuminated by a  $p$ -polarized evanescent wave generated by total internal reflection [Fig. 2(b)]. The respective projection of the incident ( $\mathbf{k}_{i\parallel}$ ) and detected ( $\mathbf{k}_{d\parallel}$ ) wave vectors are represented by white arrows. The  $4$   $\mu\text{m} \times 4$   $\mu\text{m}$  SNOM image has been obtained by lock-in detection (amplitude channel) at the  $f$  frequency. It has been shown that fringes similar to those observed in Fig. 3 correspond to the description of the phase of the incident evanescent wave relative to the position of the detector.<sup>21</sup> The fringes are oriented as if they acted as a mirror reflecting  $\mathbf{k}_{i\parallel}$  to

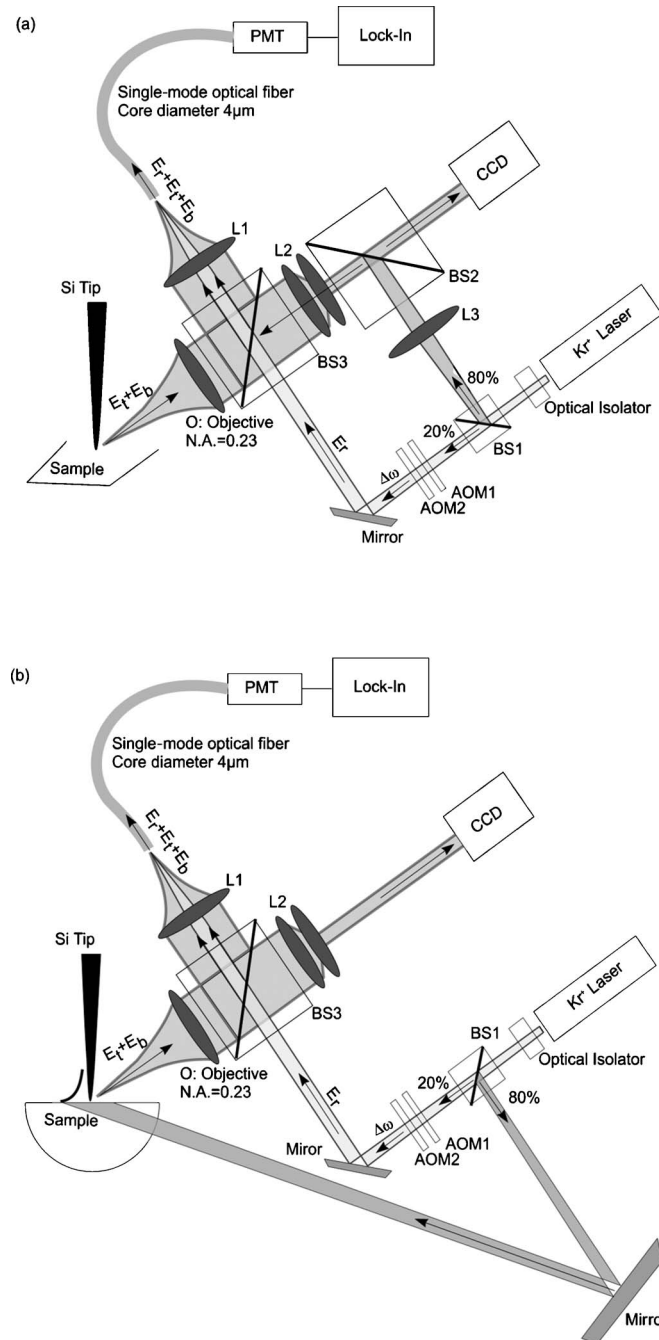


Fig. 2. (a) Details of the reflection-mode backscattered heterodyne setup. The incident light from a Kr-ion laser is split into two beams by BS1. The transmitted beam, i.e., the reference field  $E_r$ , is frequency shifted by two crossed acousto-optical cells and is coupled to a single-mode fiber. The beam reflected from BS1 is directed through a lens combination (L3 and L1) and is focused on the tip extremity by the objective O. The scattered light originating from the tip-sample ( $E_t + E_b$ ) is collected by the same objective O and is partially coupled to the optical fiber. The remaining fraction of the scattered light is imaged on a CCD camera for alignment purposes. The signals  $E_t$ ,  $E_b$ , and  $E_r$  then interfere in the fiber, and the modulation is lock-in detected (b) Details of the heterodyned apparatus for an evanescent illumination of the tip-sample. The evanescent excitation is performed through total internal reflection inside an hemispherical lens. The heterodyne detection is essentially the same as in (a).

$\mathbf{k}_{d1}$ . In Fig. 3, the interferometric term (the second term) of Eq. (3) clearly dominates. The presence of the structure perturbs the system of fringes, in a manner similar to far-field microscopy based on interferometry.<sup>28</sup> Any such local perturbation is valuable because it corresponds to the near-field perturbation of  $\phi_t - \phi_b$  in Eq. (3). As a result, Fig. 3 represents the near-field optical phase image of the sample surface. The gold wire appears dark because of a

probable destructive interference between the background field and the field scattered by the tip extremity. Precise information about the fields is, however, difficult to obtain. If we consider that  $\phi_b$  is constant during scanning,  $\phi_t$  can be modified by the relief of the sample as well as its local dielectric constant. In addition, the second term of Eq. (3) can also be sensitive to the variation of the amplitude of  $E_t$ . As a result, the optical contrast sur-

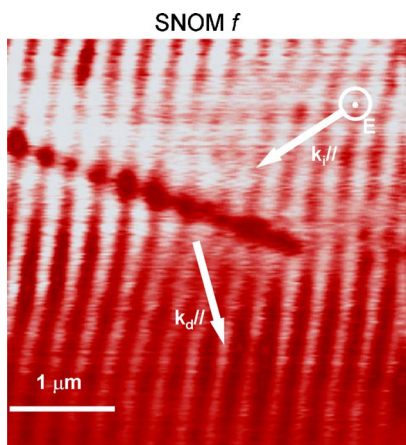


Fig. 3. (Color online) ASNOM image of a gold nanowire obtained with homodyne detection. The sample was illuminated using the evanescent excitation depicted in Fig. 2(b). The incident beam is  $p$  polarized, and the signal was demodulated (amplitude channel) at the tapping frequency  $f$ . The arrows represent the orientations of the projection on the sample surface of incident wave vector  $\mathbf{k}_{i||}$  and the detected wave vector  $\mathbf{k}_{d||}$ .

rounding the location of the gold wire should be viewed as a combination of the field amplitude, the field phase, and the topography. Furthermore,  $E_r$  can change during scanning, making the nature of the contrast randomly different.<sup>21</sup> Consequently, the image of Fig. 3 illustrates both the limitations and the complexity of the homodyne ASNOM configuration.

Figures 4 and 5 illustrate the general interest and motivation for pursuing the heterodyne version of the ASNOM. This study was performed using the reflection-mode configuration shown in Fig. 2(a). The sample was made by a nanoimprint lithography method, whereby a nanostructured stamp is made through electron-beam lithography and then imprinted into a film of polyurethane.<sup>29</sup> The structure consists of circular nanowells with varied diameter and periodicity. We selected an area of the sample in which the diameter of the wells was 500 nm and the center-to-center spacing was 800 nm, with a well depth of 450 nm. The polyurethane structure was coated through vapor deposition with a 5 nm layer of Ti and then a 40 nm layer of Au. Since this deposition occurred with the sample surface normal to the source, it is expected that the metal film covers the bottom of the wells and the top of the film but not the sides of the wells. Figures 4(a) and 4(b) show the scanning electron microscopy (SEM) and tapping-mode AFM images of the sample, respectively. Such metal structures are of interest in the field of plasmonics and near-field optics.<sup>30,31</sup> In each of the following ASNOM images, the projection (onto the sample surface) of the incident and detection wave vectors as well as the polarization of the incident field ( $E$ ) and that of the analyzed field ( $A$ ) will be represented with black arrows. It should be reiterated that the selection of the detection polarization is enabled by the adjustment of the direction of polarization of the reference field (see Section 3). This is why no polarization analysis is performed in the case of homodyne imaging. Figure 4(c) is a homodyne  $3 \mu\text{m} \times 3 \mu\text{m}$  ASNOM image (amplitude) recorded at frequency  $f$  using the configuration shown in Fig. 2(a). Similar to

Fig. 3, we observe a fringe system locally perturbed by the holes. This perturbation has to be evaluated with regard to a nonperturbed fringe system obtained on sample zones without any holes [Fig. 4(d)]. Since the sample has a significant surface profile, the background was high, and it is not surprising that the interferometric term of Eq. (3) highly dominates in Fig. 4(c). Again, the direction of the fringes corresponds to a mirror reflecting  $\mathbf{k}_{i||}$  to  $\mathbf{k}_{d||}$ . Similar to Fig. 3, it is difficult to evaluate the respective weight of the topography and the optical effects in Fig. 4(c). In Fig. 4(e), the use of the  $2f$  harmonic allows for description of near-field effects with a higher contrast<sup>16,17</sup> while maintaining the complex interferometric nature of the ASNOM signal.

Figure 5 shows ASNOM images of the nanowells by using the heterodyne version of the detection. Clear and significant improvement in the detection of the optical near

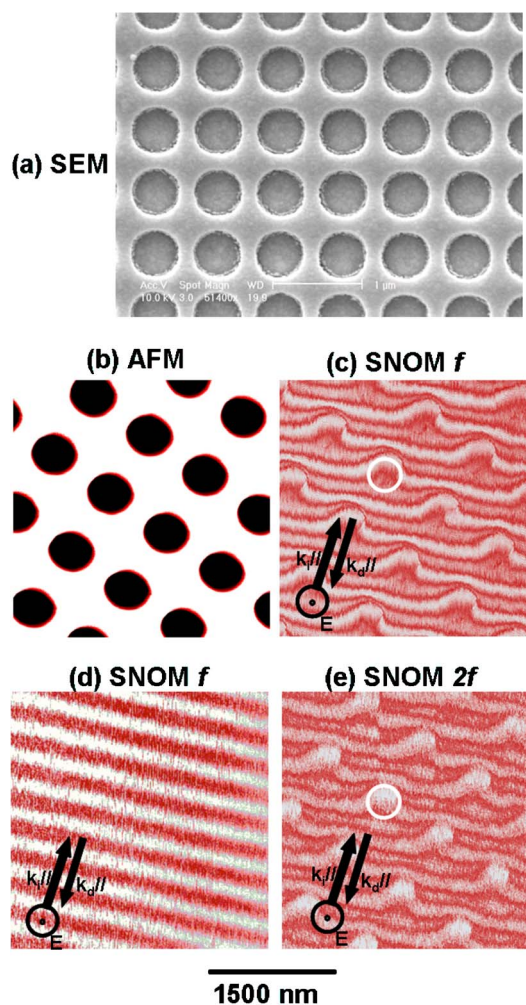


Fig. 4. (Color online) Homodyned ASNOM images of the nanowells. (a) SEM image of the nanowells. (b) Topography of the wells obtained by tapping-mode AFM. (c) Homodyne detection of the amplitude signal obtained by demodulating the scattered intensity at the tapping frequency  $f$  for an incident  $p$  polarization. The arrows represent the orientations of the incident wave vector  $\mathbf{k}_{i||}$  and the detected wave vector  $\mathbf{k}_{d||}$ . The white circle indicates the perturbation of the fringes by the well. (d) ASNOM image of a sample zone without any holes. The image was obtained under the same condition as for (c). (e) Demodulation of the scattered intensity at  $2f$ .

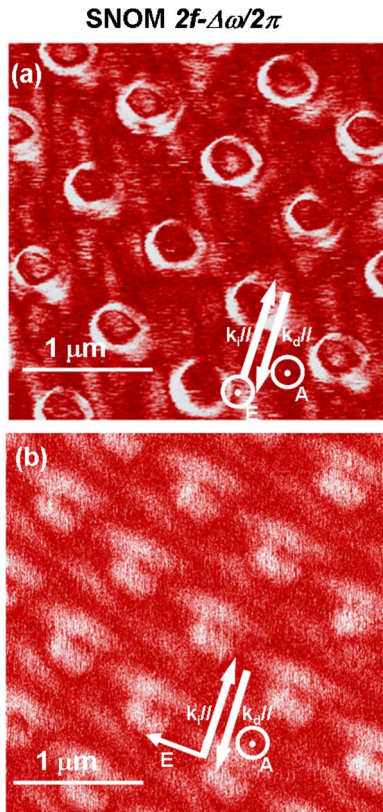


Fig. 5. (Color online) Heterodyne ASNOm images of the nanowells. (a) Heterodyne amplitude signal obtained by demodulating the detected intensity at the frequency  $(2\Omega - \Delta\omega)/2\pi = 100$  kHz. The arrows represent the orientations of the incident wave vector  $\mathbf{k}_i$  and the detected wave vector  $\mathbf{k}_d$ . The incident beam is  $p$  polarized, and the scattered signal is also detected along the  $p$  direction. (b) Same configuration as in (a) with an  $s$ -excitation polarization and a signal detected at  $p$ .

field is present. We obtained optical images by performing lock-in detection (amplitude channel) at the frequency  $(2\Omega - \Delta\omega)/2\pi = 100$  kHz. As shown in expression (7), the signal is thus proportional to the modulus of the field scattered by the tip end, without any phase information. This is confirmed by the absence of fringes in Fig. 5(a). In the literature on ASNOm, it is surprising to note that the fringes appearing in homodyne ASNOm were both reported and interpreted only by Aubert *et al.*<sup>21</sup> and that the ability of the heterodyne approach to remove the fringes was not illustrated. Figure 5(a) was obtained with  $p$  illumination (incident polarization parallel to the incident plane) and  $p$  detection (only the scattered light whose polarization is in the incident plane was detected). For an illumination that is  $s$  polarized (incident polarization perpendicular to the incident plane) and a  $p$ -polarized detection, the image represents the near field locally depolarized by the nanowells as shown in Fig. 5(b). No valuable images were obtained with  $s$ -polarized detection, in agreement with the fact that ASNOm is mainly sensitive to the component of the electric field oriented along the axis of the tip.<sup>12</sup>

The origins of the contrast mechanisms of Figs. 5(a) and 5(b) are now discussed. The geometry of the problem is illustrated by Fig. 6(a), where the edge of the nanowell is outlined by a white circle. The arrows represent the ori-

entation of the incident beam as well as the different polarization cases illustrated in Figs. 6(b)–6(e). In the case of  $p$  illumination, the edge of the well acts like a geometric singularity with regard to the incident field. The field direction is suitable to create an electromagnetic confinement<sup>32</sup> (FE). The FE effect involves mainly the field component perpendicular to the surrounding dielectric medium (air)–metal (gold) corner interface. This component is discontinuous at the dielectric–metal boundary and is associated with the surface charge density.<sup>32,33</sup> In the case of  $p$  polarization, the incident light drives the free electrons of the metal along the axis of the corner of the edge, and an increase in surface charge density is induced at the edge. Figures 6(b) and 6(c) show schematically the direction of the incident  $p$ -polarized field with regard to the gold corner at two different positions  $p_1$  and  $p_2$  along the edge. These figures illustrate that the FE occurs at every part of the edge because the projection of the incident field along the corner axis is significant everywhere at the edge. As a result, a field localization occurs on the whole edge of the nanowells, leading to bright rings that were experimentally observed [see Fig. 5(a)]. These rings correspond to an increased near-field response whose polarization remains in the incident plane.

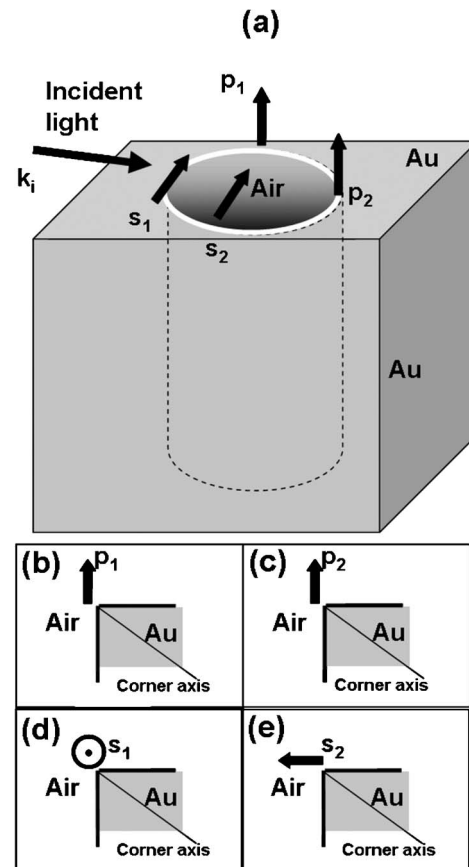


Fig. 6. (a) Sketch of the geometry. The white circle represents the rim of the well, and the labels  $p_1, p_2, s_1$ , and  $s_2$  indicate the location of different polarization cases considered in (b) to (e). (b) and (c) Schematics of the corner axis for a  $p$  polarization at the points labeled  $p_1$  and  $p_2$ . (d) and (e) Schematics of the corner axis for a  $s$  polarization at the points labeled  $s_1$  and  $s_2$ .

In the case of incident  $s$  polarization, different cases have to be considered. Case 1 is labeled  $s_1$  in Fig. 6(a) and 6(d). In that configuration, the incident field is mainly tangential to the edge, and the local field vanishes both inside and outside the corner. The foremost end of the edge remains thus unchanged. A second example is called  $s_2$  in Figs. 6(a) and 6(e). Here, unlike  $s_1$ , the incident field has a significant projection onto the corner axis. Consequently, in the case of  $s$  polarization, the field amplitude is expected to be nonuniform over the border of the wells, as observed experimentally in Fig. 5(b).

To get more precise information about the field in the vicinity of the wells, we performed three-dimensional electromagnetic calculations based on the finite-difference time-domain (FDTD) method.<sup>34</sup> This method has proved to be fruitful for solving several near-field optical problems.<sup>13,35,36</sup> The FDTD method is a flexible numerical means of solving Maxwell's differential equations in both time and space for arbitrary system configurations. In Fig. 7 the results of an FDTD study on an array of nanowells similar to the experimental configuration are presented. Specifically, thin 5 nm Ti and 40 nm Au films are placed on top of a polymer, and holes of diameter 500 nm and well depth of 450 nm are created at the top of the gold film. Finally, 5 nm Ti and 40 nm Au coatings are placed on the bottom of each well. The center-to-center hole distance is 647.4 nm. The wavelength of incident light is 647.4 nm. The Au metal is described by a Drude model with parameters obtained by fitting the empirical dielectric constants of bulk Au material at wavelengths close to 647.4 nm.<sup>35,36</sup> To absorb waves approaching the numerical grid edges, the film is truncated with a uniaxial perfect matching layer.<sup>32</sup> A film of area  $6\ \mu\text{m} \times 6\ \mu\text{m}$  contain-

ing a square array of  $7 \times 7$  nanowells is considered in our calculations. We subsequently display and discuss just the central  $3 \times 3$  nanowell portion, which should be relatively free of edge effects. A total field-scattered field method<sup>34</sup> is used to launch the incident light at an angle of  $75^\circ$  from the normal to the metal surface, which corresponds to the experimental configuration. The incident light corresponds to a plane wave of wavelength 647.4 nm multiplied by a flat-top Gaussian function as in Ref. 35 to create a  $3\ \mu\text{m}$  diameter beam spot. In the calculated images, the incident electromagnetic wave propagates from bottom to top. For incident light with  $p$  polarization, where the incident electric field has a significant component normal to the surface, high intensity is seen all along the edges of the nanowells, leading to bright rings as shown in Figs. 7(a) and 7(b), which represent, respectively, the magnitude of the total field and the surface normal field component at the sample plane. This is most likely due to the discontinuity of the normal component near the edges of the wells. We also note that the polarization of the near field of the nanowells is mainly longitudinal, that is, parallel to the tip [see Fig. 7(b)]. This can explain why high contrast near-field images were obtained using  $p$ -polarized detection: this contrast is believed to be enhanced by a lightning rod effect that occurs at the tip extremity.<sup>20</sup> Bright spots localized between the wells predicted by Fig. 7(b) are not visible in Fig. 5(a) because the microscope is principally sensitive to evanescent waves, whereas the bright spot has been shown to be mainly made of propagating waves (bright rings correspond to confined evanescent fields). For incident light with  $s$  polarization where the incident electric field is parallel to the surface, the intensity is lower, and its distri-

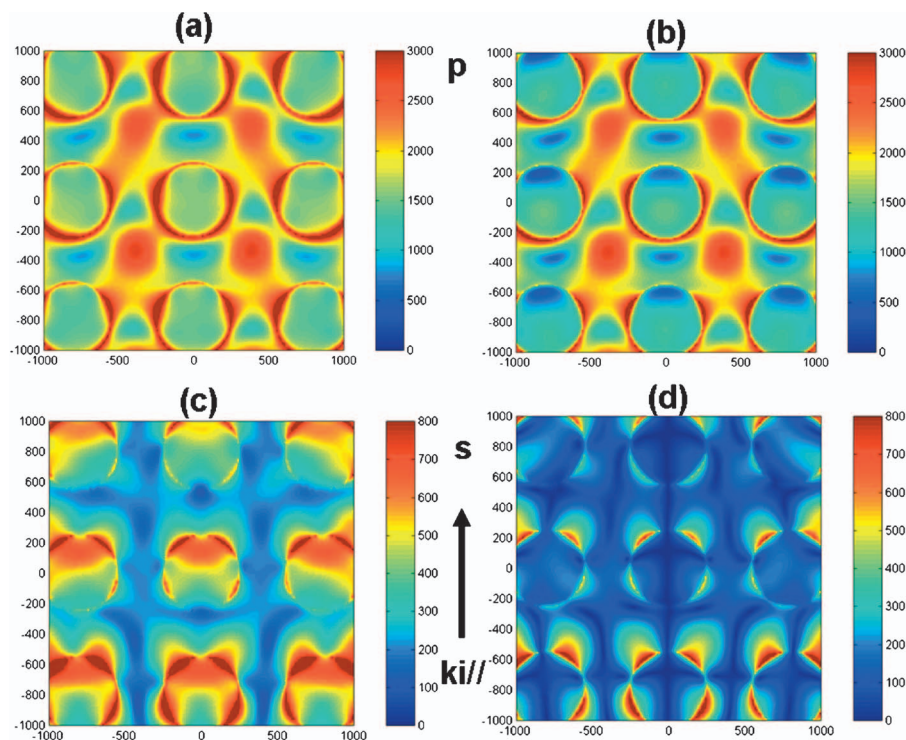


Fig. 7. Three-dimensional FDTD results ( $2\ \mu\text{m} \times 2\ \mu\text{m}$  calculated images). The arrows represent the projection of the incident wave vector: (a)  $p$  incident polarization, magnitude of the total field at the sample surface; (b)  $p$  incident polarization, surface normal component; (c)  $s$  incident polarization, magnitude of the total field; (d)  $s$  incident polarization, normal component.

bution is not uniform on the sides of the nanowells, as shown in Figs. 7(c) and 7(d). Additionally, the surface normal near field [Fig. 7(d)], corresponding to local light depolarization, has a low intensity compared with Fig. 7(b), possibly explaining why the obtained images have less contrast.

As a result, the heterodyne version of the ASNOm both increases near-field sensitivity and allows for detection of the actual field amplitude in the presence of high background light, independently of the phase.

Approach curves have confirmed that the amplitude of the near electromagnetic field can be detected by heterodyne ASNOm, without the mixing with phase or intensity highlighted by Eq. (3). A total internal reflection experiment was performed within a prism (refraction index  $n_p = 1.5$ ), and the resulting evanescent wave was detected by ASNOm [see configuration of Fig. 2(b)]. The incident wave ( $\lambda = 647.4$  nm) was  $p$  polarized, and the angle incidence  $\theta$  was  $\sim 55^\circ$  (larger than the critical angle). The amplitude of the field is then given by

$$E(z) = E_o \exp(-z/d_p), \quad (8)$$

where  $z$  is the distance to the prism surface and  $d_p$  is the field penetration depth given by

$$d_p = \frac{\lambda}{2\pi(n_p^2 \sin^2 \theta - n_{\text{air}}^2)^{1/2}}, \quad (9)$$

where  $n_{\text{air}}$  is the air refraction index ( $\sim 1$ ). For this experimental configuration, we estimate that  $d_p$  is approximately 144 nm.

The intensity  $I$  is thus given by

$$I(z) = E_o^2 \exp(-2z/d_p). \quad (10)$$

$I$  is associated with an apparent decay length, which is half that of the amplitude (i.e.,  $\sim 72$  nm).

In the case of homodyne ASNOm, approach curves do not describe  $E$  or  $I$  but rather a subtle mixing of both of them.<sup>21</sup> As a result, tip position and environment can produce different approach curves with various apparent decay lengths  $\geq d_p/2$ . Additionally, the measured approach curve is not exponential-like if destructive interferences occur between tip field and background field.<sup>21</sup>

By performing lock-in detection at  $f$  and  $2f$ , we observed the above effect, which illustrates the limits of the homodyne ASNOm. However, as a complementary experiment, we measured approach curves at  $f - \Delta\omega/2\pi$ . In that case, approach curves were noted to be exponential-like and constant at all tip positions. Figure 8(a) shows an approach curve obtained at  $f - \Delta\omega/2\pi$ . It is exponential with a decay length of  $\sim 145 \pm 5$  nm, characteristic of the field amplitude rather than the intensity. Similar approach curves were obtained for different tip positions. For example, Fig. 8(b) shows an approach curve, measured at a  $2 \mu\text{m}$  distance from the position for Fig. 8(a). Figure 8(b) presents the decay length of the field amplitude ( $140 \pm 5$  nm). On the other hand, approach curves measured at  $f$  exhibit a dependence on both the tip position and the environment. As an example, Fig. 8(c) is an approach curve measured at frequency  $f$  in a sample zone with low roughness. The apparent decay length was measured to be  $65 \pm 5$  nm, characteristic of the intensity of the

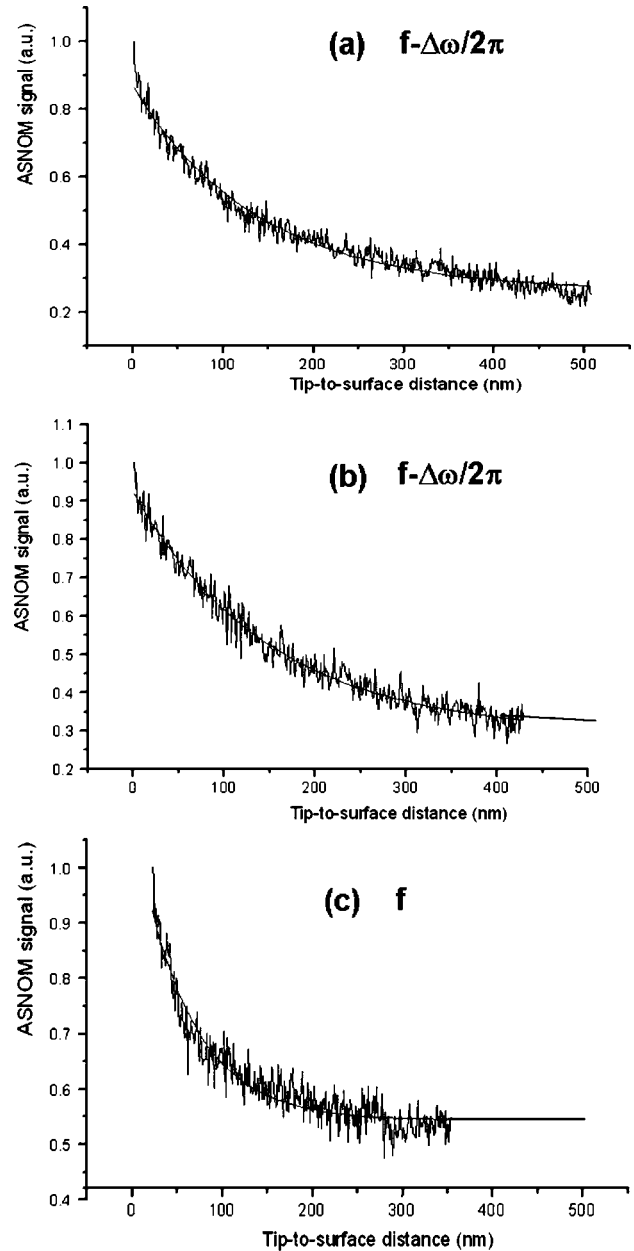


Fig. 8. Approach curves recorded above a prism in which a total internal reflection was performed. ASNOm signal (from the amplitude channel of the lock-in amplifier, arbitrary units) as a function of the average distance between the vibrating probe and the prism surface. Field depth penetration was  $d_p = 144$  nm. (a) Signal demodulated at frequency  $f - \Delta\omega/2\pi$ . Apparent depth penetration  $\sim d_p$ . (b) Signal demodulated at frequency  $f - \Delta\omega/2\pi$ . The tip was placed at a  $2 \mu\text{m}$  distance from the position for (a). Apparent depth penetration  $\sim d_p$ . (c) Signal demodulated at frequency  $f$ . The background was low because the tip was placed at a clean zone. Apparent depth penetration  $\sim d_p/2$ .

field rather than its amplitude. In that case the intrinsic interferometric effect is believed to be negligible (because of a low background), and the ASNOm signal described mainly the intensity [the first term of Eq. (3) dominates]. As a result, Fig. 8 confirms that the heterodyne ASNOm allows for extraction of the actual field amplitude, without any phase information.

## B. Phase Imaging

In Subsection 4.A we focused our attention on amplitude images and did not present any phase images whose interpretation is underway. Clear phase imaging was, however, performed on optical integrated waveguides. The studied sample was a single-mode buried integrated waveguide similar to that recently studied by homodyne ASNM.<sup>21,37,38</sup> The guide was produced by the ion-exchange technique described in Ref. 39. The heterodyne ASNM configuration was similar to that sketched in Fig. 2(b) except that the beam 80% reflected by BS1 was launched into the integrated waveguide. Moreover, a semiconductor infrared laser was used as a source (wavelength=1.55  $\mu\text{m}$ ). The tip was scanned above the top of the guide and scattered the evanescent field generated by total internal reflection within the guide. We assume that the AFM probe is passive and thus that the scattered field is proportional to the guided field. Figure 9(a) shows the AFM image of the guide. Figure 9(b) shows the corresponding homodyne SNOM image obtained by lock-in demodulation at the probe oscillation frequency  $f$  [involving wave vectors that are shown in Fig. 9(a)]. In that case, as shown in Subsection 2.A, a homodyne interferometric signal is detected in addition to the intensity signal related to the probe (and the guided wave). The local phase variation of the field scattered by the tip is hence converted into amplitude modulation, and the related phase shift in Eq. (3) leads to oblique fringes ap-

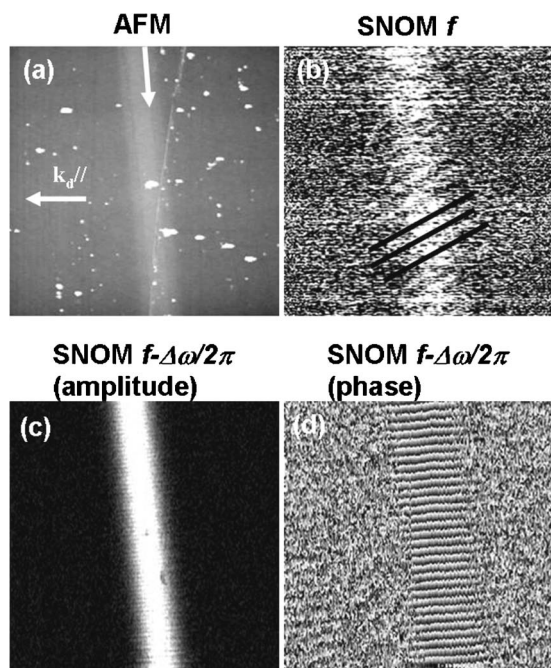


Fig. 9. Near-field images of  $10 \mu\text{m} \times 10 \mu\text{m}$  of a buried ion-exchanged waveguide. (a) AFM image. The image height range is 70 nm, and the guide height is 20 nm. The white arrows represent the respective projection of the incident and detection wave vectors used for the optical analysis. (b)–(d) ASNM images at  $\lambda = 1.55 \mu\text{m}$ . (b) ASNM image obtained by lock-in detection (amplitude channel) at frequency  $f$ . The black segments highlight the oblique fringes. (c) ASNM image obtained by lock-in detection (amplitude channel) at frequency  $f - \Delta\omega/2\pi$ . (d) ASNM image obtained by lock-in detection (phase channel) at frequency  $f - \Delta\omega/2\pi$ .

pearing on the experimental image [see Fig. 9(b)]. This phenomenon was reported in Ref. 21. However, with lock-in demodulation frequency set to  $(\Omega - \Delta\omega)/2\pi$ , it is noticeable that the unmodulated background contribution cancels (see Subsection 2.B). Figures 9(c) and 9(d) demonstrate this effect. Figure 9(c) depicts the image provided by the amplitude channel of the lock-in amplifier, and Fig. 9(d) shows the lock-in phase image. A clear separation of the optical phase and amplitude is achieved, in agreement with results from Refs. 11, 22, and 23. The fringes related to the mix between  $E_b$  and  $E_t$  actually vanished. We can also notice in the amplitude image a quasi standing-wave issued from interference between a forward-guided wave and a backward wave that was Fresnel-reflected at the output facet. In addition, a comparison between the intensity image [Fig. 9(b)] and the amplitude image [Fig. 9(c)] shows an increase of the signal level, which is expected from the heterodyne detection scheme, since  $|E_t|$  is multiplied by a factor  $|E_r|$  [see expression (7)]. In the case of Fig. 9(b), the signal-to-noise ratio was dominated by Johnson noise (thermal electronic noise), and the minimum detected optical power was of the order of  $10^{-12}$  W. In the case of the data image [Fig. 9(c)], we achieved a shot-noise-limited detection (about  $10^{-17}$  W), since the total optical power seen by the photodetector was enhanced sufficiently by the reference power. This allowed us to use a simple GaAs photodiode instead of a photomultiplier detector or an avalanche photodiode, contributing to reduced electronic noise. In Fig. 9(d), the wavefront of the guided field is clearly visible. Analysis of such an image can lead to determination of propagation constants.<sup>40</sup> As a conclusion of Subsection 4.B, the heterodyne version of the ASNM has been shown to be able to extract both phase and amplitude of the near field, independently of each other. It is obvious that this capability is of great physical interest, since it provides a direct and nondestructive way to quantify waveguide optical parameters such as propagation constants, mode profiles, and propagation losses.<sup>41</sup>

In conclusion, through several examples, we have shown that implementing heterodyne interferometry is an efficient way to both overcome problems related to the background field in coherent apertureless scanning near-field microscopy and get field amplitude and phase with subwavelength resolution. From a general point of view, the heterodyne ASNM turns out to be a powerful tool for characterization of modern components in integrated optics.

## ACKNOWLEDGMENTS

The authors at Université de Technologie de Troyes acknowledge the Conseil Régional de Champagne-Ardennes and the European Social Funds for financial support. A. Bouhelier acknowledges support from the Office of Basic Energy Sciences, Division of Materials Sciences, U.S. Department of Energy under contract W-31-109-ENG-38. This work also benefited from the Consortium for Nanoscience Research.

Corresponding authors G. P. Wiederrecht and R. Bachelot can be reached by e-mail at wiederrecht@anl.gov and renaud.bachelot@utt.fr.

\*Current address, Laboratoire de Physique de l'Université de Bourgogne, UMR 5027, 9 Avenue Alain Savary, BP47870. F-21078 Dijon Cedex, France.

## REFERENCES

1. D. W. Pohl, W. Denk, and M. Lanz, "Optical stethoscopy: image recording with resolution  $\lambda/20$ ," *Appl. Phys. Lett.* **44**, 651–653 (1984).
2. M. A. Paesler and P. J. Moyer, *Near-Field Optics* (Wiley, 1996).
3. J. P. Fillard, *Near-field Optics and Nanoscopy* (World Scientific, 1996).
4. D. Courjon and C. Bainier, eds., *Le Champ Proche Optique. Théorie et applications* (Springer-Verlag France and France Télécom R&D, 2001).
5. J. Wessel, "Surface-enhanced optical microscopy," *J. Opt. Soc. Am. B* **2**, 1538–1540 (1985).
6. W. Denk and D. W. Pohl, "Near-field optics: microscopy with nanometer-size fields," *J. Vac. Sci. Technol. B* **9**, 510–513 (1991).
7. Y. Inouye and S. Kawata, "Near-field scanning optical microscope with a metallic probe tip," *Opt. Lett.* **19**, 159–161 (1994).
8. F. Zenhausern, M. P. O'Boyle, and H. K. Wickramasinghe, "Apertureless near-field optical microscope," *Appl. Phys. Lett.* **65**, 1623–1625 (1994).
9. R. Bachelot, P. Gleyzes, and A. C. Boccara, "Near-field optical microscopy by local perturbation of a diffraction spot," *Microsc. Microanal. Microstruct.* **5**, 389–397 (1994).
10. R. Bachelot, P. Gleyzes, and A. C. Boccara, "Near-field optical microscope based on local perturbation of a diffraction spot," *Opt. Lett.* **20**, 1924–1926 (1995).
11. R. Hillenbrand, F. Keilmann, P. Hanarp, D. S. Sutherland, and J. Aizpurua, "Coherent imaging of nanoscale plasmon patterns with a carbon nanotube optical probe," *Appl. Phys. Lett.* **83**, 368–370 (2003).
12. S. Patané, G. P. Gucciardi, M. Labardi, and M. Allegrini, "Apertureless near-field optical microscopy," *Riv. Nuovo Cimento* **27**, 1–46 (2004).
13. G. A. Wurtz, J. S. Im, S. K. Gray, and G. P. Wiederrecht, "Optical scattering from isolated metal nanoparticles and arrays," *J. Phys. Chem. B* **107**, 14191–14198 (2003).
14. A. Lahrech, R. Bachelot, P. Gleyzes, and A. C. Boccara, "Infrared-reflection-mode near-field microscopy using an apertureless probe with a resolution of  $\lambda/600$ ," *Opt. Lett.* **21**, 1315–1317 (1996).
15. T. Taubner, R. Hillenbrand, and F. Keilmann, "Performance of visible and mid-infrared scattering-type near-field optical microscopes," *J. Microsc.* **210**, 311–314 (2003).
16. G. Wurtz, R. Bachelot, and P. Royer, "Imaging a GaAlAs laser diode in operation using apertureless scanning near-field optical microscopy," *Eur. Phys. J.: Appl. Phys.* **5**, 269–275 (1999).
17. R. Hillenbrand, B. Knoll, and F. Keilmann, "Pure optical contrast in scattering-type scanning near-field microscopy," *J. Microsc.* **202**, 77–83 (2000).
18. V. Sandoghdar, J. Michaelis, C. Hettich, C. Schmitt, J. Zitzmann, and S. Kühn, "Results and thoughts on optical microscopy using a single-molecule probe," *Single Mol.* **2**, 277–281 (2001).
19. L. Aigouy, Y. De Wilde, M. Mortier, J. Giérak, and E. Bourhis, "Fabrication and characterization of fluorescent rare-earth-doped glass-particle-based tips for near-field optical imaging applications," *Appl. Opt.* **43**, 3829–3837 (2004).
20. A. Bouhelier, M. R. Beversluis, and L. Novotny, "Applications of field-enhanced near-field optical microscopy," *Ultramicroscopy* **100**, 413–419 (2004).
21. S. Aubert, A. Bruyant, S. Blaize, R. Bachelot, G. Lerondel, S. Hudlet, and P. Royer, "Analysis of the interferometric effect of the background light in apertureless scanning near-field optical microscopy," *J. Opt. Soc. Am. B* **20**, 2117–2124 (2003).
22. R. Hillenbrand and F. Keilmann, "Complex optical constants on a subwavelength scale," *Phys. Rev. Lett.* **85**, 3029–3032 (2000).
23. T. Taubner, R. Hillenbrand, and F. Keilmann, "Nanoscale polymer recognition by spectral signature in scattering infrared near-field microscopy," *Appl. Phys. Lett.* **85**, 5064–5066 (2004).
24. S. Ducourtieux, S. Grésillon, J. C. Rivoal, C. Vannier, C. Bainier, D. Courjon, and H. Cory, "Imaging subwavelength holes in chromium films in scanning near-field optical microscopy. Comparison between experiments and calculation," *Eur. Phys. J.: Appl. Phys.* **26**, 35–43 (2004).
25. R. Laddada, S. Benrezzak, P. M. Adam, G. Viardot, J. L. Bijeon, and P. Royer, "Detection of an evanescent field scattered silicon tips in an apertureless scanning near-field optical microscope," *Eur. Phys. J.: Appl. Phys.* **6**, 171–178 (1999).
26. J. N. Walford, J. A. Porto, R. Carminati, J.-J. Greffet, P. M. Adam, S. Hudlet, J.-L. Bijeon, A. Stashkevich, and P. Royer, "Influence of tip modulation on image formation in scanning near-field optical microscopy," *J. Appl. Phys.* **89**, 5159–5169 (2001).
27. J. J. Greffet and R. Carminati, "Image formation in near-field optics," *Prog. Surf. Sci.* **56**, 133–237 (1997).
28. C. J. Koester, "Interference microscopy: theory and techniques," in *The Encyclopedia of Microscopy*, G. L. Clark, ed. (Reinhold, 1961), pp. 420–434.
29. F. Hua, Y. Sun, A. Gaur, M. A. Meitl, L. Bilhaut, L. Rotkina, J. Wang, P. Geil, M. Shim, and J. A. Rogers, "Polymer imprint lithography with molecular-scale resolution," *Nano Lett.* **4**, 2467–2471 (2004).
30. E. Hutter and J. Fendler, "Exploitation of localized surface plasmon resonance," *Adv. Mater. (Weinheim, Ger.)* **16**, 1685–1706 (2004).
31. G. P. Wiederrecht, "Near-field imaging of metal nanoparticles," *Eur. Phys. J.: Appl. Phys.* **28**, 3–18 (2004).
32. J. Van Bladel, *Singular Electromagnetic Fields and Sources* (IEEE, 1995).
33. J. A. Stratton, *Electromagnetic Theory* (McGraw-Hill, 1941).
34. A. Taflove and S. C. Hagness, *Computational Electrodynamics: The Finite Difference Time-domain Method*, 2nd ed. (Artech House, 2000).
35. S. K. Gray and T. Kupka, "Propagation of light in metallic nanowire arrays: finite-difference time-domain results for silver cylinders," *Phys. Rev. B* **68**, 045415 (2003).
36. S.-H. Chang, S. K. Gray, and G. C. Schatz, "Surface plasmon generation and light transmission by isolated nanoholes and arrays of nanoholes in thin metal films," *Opt. Express* **13**, 3150–3155 (2005).
37. R. Bachelot, G. Lerondel, S. Blaize, S. Aubert, A. Bruyant, and P. Royer, "Probing photonic and optoelectronic structures by apertureless scanning near-field optical microscopy," *Microsc. Res. Tech.* **64**, 441–452 (2004).
38. S. Blaize, S. Aubert, A. Bruyant, R. Bachelot, G. Lerondel, P. Royer, J. M. Broquin, and V. Minier, "Apertureless scanning near-field optical microscopy for ion exchanged channel waveguide characterization," *J. Microsc.* **209**, 155–161 (2003).
39. J.-E. Broquin, "Ion-exchange integrated devices," in *Integrated Optical Devices V*, V. Giancarlo, C. Righini, and S. Honkanen, eds., *Proc. SPIE* **4277**, 105–115 (2001).
40. I. Sefanon, S. Blaize, A. Bruyant, S. Aubert, G. Lerondel, R. Bachelot, and P. Royer, "Heterodyne detection of guided waves using a scattering-type Scanning Near-Field Optical Microscope," *Opt. Express* **13**, 5553–5564 (2005).
41. M. L. M. Balistreri, J. P. Korterik, L. Kuipers, and N. F. van Hulst, "Phase mapping of optical fields in integrated optical waveguide structures," *J. Lightwave Technol.* **19**, 1169–1176 (2001).